Queen's University Belfast

Magnetic short-range order in the new ternary phase Mn8Pd15Si7

Eriksson, T., Mellergard, A., Nordblad, P., Larsson, A. K., Felton, S., Howing, J., ... Andersson, Y. (2005). Magnetic short-range order in the new ternary phase Mn8Pd15Si7. Journal of Alloys and Compounds, 403(1-2), 19-28. DOI: 10.1016/j.jallcom.2005.04.202

Published in:
Journal of Alloys and Compounds

Document Version:
Peer reviewed version

Queen's University Belfast - Research Portal:
Link to publication record in Queen's University Belfast Research Portal

Publisher rights
© 2005 Elsevier Ltd. This manuscript version is made available under the CC-BY-NC-ND 4.0 license
http://creativecommons.org/licenses/by-nc-nd/4.0/which permits distribution and reproduction for non-commercial purposes, provided the author and source are cited.

General rights
Copyright for the publications made accessible via the Queen's University Belfast Research Portal is retained by the author(s) and / or other copyright owners and it is a condition of accessing these publications that users recognise and abide by the legal requirements associated with these rights.

Take down policy
The Research Portal is Queen's institutional repository that provides access to Queen's research output. Every effort has been made to ensure that content in the Research Portal does not infringe any person's rights, or applicable UK laws. If you discover content in the Research Portal that you believe breaches copyright or violates any law, please contact openaccess@qub.ac.uk.

Download date:16. Feb. 2017

Magnetic short-range order in the new ternary phase $Mn_8Pd_{15}Si_7$

T. Eriksson[a], A. Mellergård[b], P. Nordblad[c], A.-K. Larsson[d], S. Felton[c], J. Höwing[a], T. Gustafsson[a], Y. Andersson[a,*]

[a]*Dept. Materials Chemistry, Uppsala University, box 538, SE-751 21 Uppsala, Sweden*

[b]*Studsvik Neutron Research Laboratory, Uppsala University, SE-611 82 Nyköping, Sweden*

[c]*Dept. Engineering Sciences, Uppsala University, box 534, SE-751 21 Uppsala, Sweden*

[d]*Research School of Physical Science, Dept. Applied Mathematics, Australian National University, Canberra, Australia*

A new compound, $Mn_8Pd_{15}Si_7$, is reported to crystallize in a face centered cubic unit cell of dimension a=12.0141(2) Å, space group $Fm\bar{3}m$, and can thus be classified as a G-phase. The crystal structure was studied by single crystal x-ray diffraction, x-ray and neutron powder diffraction and electron diffraction. A filled $Mg_6Cu_{16}Si_7$ type structure was found, corresponding to the $Sc_{11}Ir_4$ type structure. The magnetic properties were investigated by magnetization measurements and Reverse Monte Carlo modeling of low temperature magnetic short-range order. Dominating near neighbor antiferromagnetic correlations were found between the Mn atoms and geometric frustration in combination with random magnetic interactions via metal sites with partial Mn occupancy were suggested to hinder formation of long-range magnetic order.

Keywords: (A) Intermetallics, (C) Neutron powder diffraction, (C) X-ray diffraction, (D) Magnetic measurements.

* Corresponding author. E-mail address: yvonne.andersson@mkem.uu.se
Telephone: +46-18-4713780; Fax: +46-18-513548

Introduction

Compounds containing manganese often show interesting, complicated magnetic structures. For example we have recently reported on frustrated magnetic interactions on a triangular network of Mn atoms, resulting in a 120° spin configuration, for the new phases Mn_3IrSi [1] and Mn_3IrGe [2]. Geometric frustration of antiferromagnetic interactions also arises when the magnetic atoms are situated on the corners of octahedra (see Fig. 1a), as is the case in the Cu_3Au type compounds Mn_3Rh, Mn_3Pt and Mn_3Ir. In these the Mn magnetic moments lie in the (111) plane and point in ⟨211⟩ directions, forming 120° angles, see Fig. 1b (D-phase) [3-6]. For Mn_3Pt a second antiferromagnetic phase (F-phase) [5] is formed just below the Néel temperature, where the frustration is suppressed as two of the six spins on the octahedron are rapidly fluctuating and thus appear to be non-magnetic [7]. Another example of antiferromagnetic interactions on Mn_6-octahedra is provided by $Mn_6Ni_{16}Si_7$ [8], which crystallizes with the $Mg_6Cu_{16}Si_7$ type structure [9,10] (space group $Fm\bar{3}m$) with the octahedra at the face centers and corners of the unit cell. Here the proposed model of magnetic order is that four of the magnetic moments on one octahedron (situated in a common plane) are coupled ferromagnetically and the remaining two (situated above and below the plane) show the opposite moment direction, with octahedra in alternating sheets coupled antiferromagnetically [8].

This article reports on the preparation, crystal structure determination and magnetic properties of a new metal rich Pd-Mn-Si phase, namely $Mn_8Pd_{15}Si_7$, with a crystal structure similar to that of $Mn_6Ni_{16}Si_7$. The crystal structure has been investigated by single crystal x-ray diffraction, electron diffraction, neutron and x-ray powder diffraction. Reverse Monte Carlo modeling of magnetic short-range order has been performed, based on neutron powder diffraction data, and the magnetic properties have been studied by SQUID magnetometry.

Reverse Monte Carlo (RMC) modeling is a useful tool for analysis of short range order (SRO) in condensed matter [11]. Originally developed for the study of liquids and amorphous solids it has now also been applied to local order in crystalline materials. Recently a program, RMCPOW, has been developed for modeling the local and average crystalline and magnetic structure based on powder diffraction data [12,13]. This technique has been applied to topics such as magnetic SRO in MnO [14], spin frustration in the Kagomé system SrCrGaO [15] and local and average magnetic order in simple and double perovskite systems [16-18]. Similar methods have been used to investigate the magnetic SRO in the β-manganese system [19]. Common to all these studies is the approach to go beyond the average crystallographic picture and use the information in the diffuse scattering to investigate local ordering effects.

Experimental

Synthesis

A sample of composition 28.0 at.% Mn, 47.7 at.% Pd, 24.3 at.% Si was prepared by the drop-synthesis method [20]. The synthesis was performed in a high frequency vacuum induction furnace under 300 mbar argon atmosphere, with the sample contained in an alumina crucible. Starting materials were single crystal pieces of silicon (Highways International, purity 99.999 %), pressed pellets of palladium powder (Cerac, purity 99.95 %) and pieces of manganese metal (Cerac, claimed purity 99.99 %, purified from manganese oxides by sublimation). The sample was crushed, pressed into pellets and annealed in an evacuated fused silica tube for three days at 900°C, four days at 800°C, one month at 750°C, and finally crushed into powder and stress relieved at 650°C for 40 minutes.

X-ray diffraction

Phase analysis and unit cell refinements were performed from x-ray powder diffraction films, recorded by a Guinier-Hägg type focusing camera. Cu$K\alpha_1$ radiation was used and silicon was added as internal standard for calibration (a = 5.43088(4) Å at 25°C).

Crystals were selected from the powder and mounted for single crystal x-ray diffraction, using a STOE 4-circle diffractometer (Mo$K\alpha$ radiation). However, numerous attempts proved it difficult to find single crystals of good quality; the crystals were often agglomerates, or were severely twinned. For one single crystal fragment it was possible to obtain a unit cell, and intensity data collection was performed in the 2θ-range 10°–80°. The structure was solved by direct methods and difference Fourier synthesis, as implemented in the program suite SHELX-97 [21]. Due to problems with corrections for the high absorption and for extinction, the data set was only used for preliminary structure refinements (3794 reflections), using the program suite DUPALS [22].

X-ray powder diffraction data were collected in transmission mode on a STOE & Cie GmbH STADI powder diffractometer (Cu$K\alpha_1$ radiation), equipped with a linear position sensitive detector (6° in 2θ). Data were recorded in the 2θ-range 10°–90°, in steps of 0.02°, and used in crystal structure refinements.

Neutron powder diffraction

Neutron powder diffraction data for crystal structure refinements were collected at 295 K, in the 2θ-range 10°–140° in steps of 0.08°, on the NPD instrument at the R2 reactor, Studsvik, Sweden. The sample was placed in a vanadium cylinder and the neutron beam was monochromated to 1.471 Å using a parallel double Cu (220) monochromator system. For the

purpose of Rietveld refinement an absorption correction was applied using $\mu R = 0.164$, as calculated from a transmission measurement at $2\theta = 0°$. For the application of RMC modeling it is necessary to correct the raw data not only for absorption but also multiple scattering, inelastic effects, and instrumental background. Hence additional measurements with the empty vanadium container and cryostat were also performed. The corrections were applied, following the procedure in [23], using the program CORRECT [24] to yield the differential scattering cross-section.

An additional set of neutron powder diffraction data were collected at 295 K and 15 K in the 2θ-range 3.70° to 136.9°, on the SLAD-instrument, also at Studsvik, with the wavelength 1.116 Å. Having a higher incident neutron energy, and hence giving a more complete integration over inelastic scattering processes, data from the SLAD instrument would constitute a better estimate for a total scattering experiment than corresponding NPD data. In general, SLAD data also show better performance in the measurement of the weak diffuse scattering signal. However, due to non-standard variations of the instrument resolution width, the actual RMC modeling was performed with data from the NPD instrument and the data measured at the SLAD instrument were only used for comparison.

Crystal structure refinements

Crystal structure refinements were performed for powder diffraction data, by the Rietveld method, using the program FULLPROF [25]. The sample contained small amounts of two additional phases, Pd_2Si [26] and Mn_5Si_3 [27], which were both included in the refinements. The atom coordinates were solved from the single crystal x-ray diffraction data set, and further refined for both x-ray (single crystal and powder) and neutron powder diffraction (NPD) data sets, with the same results for all data sets. The occupancies were refined by

alternating between the different data sets. Since Mn has a negative scattering length for neutrons (and Pd a positive), neutron diffraction data give better abilities to distinguish between occupancy of Pd or Mn for one site than provided by x-ray diffraction. On the other hand, in neutron diffraction mixed occupancy of Pd and Mn can not be distinguished from partial Pd occupancy or even (for a certain ratio of Pd/Mn) from full Si occupancy, whereas x-ray diffraction gives strong contrast between Si and Pd. Thus, reliable values for the occupancies could only be found by combining x-ray and neutron diffraction data. The single crystal x-ray diffraction data set suffered from problems with correcting for high absorption and extinction in the crystal. A reliable absorption correction was also difficult to achieve for the powder x-ray diffraction data set. For neutrons, absorption is less severe and can easily be corrected for, and thus the final refinement cycles were performed only for the neutron diffraction intensities.

The used scattering lengths for neutrons were Mn: -3.73 fm, Pd: 5.91 fm, Si: 4.149 fm. The pseudo-Voigt function was used to describe the peak shape and the background was modeled by interpolation between fixed points. Since the temperature factors are strongly correlated with the occupancies, an over-all isotropic temperature factor was used, and was only varied after the values of the occupancies had converged. In the last refinement cycles, 22 parameters were varied. These were for the main phase: Profile parameters: 2θ zero point (1), scale factor (1), profile shape parameter (1), half-width parameters (3), asymmetry parameters (2); Structural parameters: atomic coordinates (3), lattice parameter (1), occupancies (3), over-all isotropic temperature factor (1). For Pd_2Si and Mn_5Si_3 only scale factors (2) and lattice parameters (4) were varied.

RMC modeling

RMC modeling is a general method to model structure by optimizing the agreement with experimental e.g. diffraction data. Similar to simulated annealing techniques a Monte Carlo procedure is used for this optimization, however, in the RMCPOW implementation not only the average crystalline structure but also the short-range order is modeled by simultaneous fitting of the Bragg and diffuse scattering. For crystalline materials the initial model is naturally chosen as a super-cell to the crystallographic unit cell. Basically, the algorithm is to calculate relevant diffraction data for the chosen model and compare to the experimental data using a χ^2 test. Atoms (spins) are selected at random and given a random displacement (rotation) and the new model scattering data is calculated. Moves are accepted if χ^2 decreases. To prevent ending up in local minima, moves resulting in increased values of χ^2 are accepted by a certain probability. This procedure is repeated until the fit converges. The proposed structure at convergence represents one possible solution.

In the current study, model configurations were built as 3×3×3 unit cells (i.e. 3240 atoms and 892 spins) with dimensions and atom positions as determined by the Rietveld refinements. Initially, Mn and Pd atoms at the mixed M1, M2 and M3 sites (see Table 1) were explicitly identified in appropriate numbers by random selection. In order to account for the nuclear thermal diffuse scattering the atomic positions were shifted from the equilibrium crystallographic sites by means of a phonon-related distribution of random displacements. Magnetic spins at the Mn positions were given a random initial orientation. All spins were assigned the same effective moment, corresponding to $g\sqrt{[S(S+1)]}$, nominally 5 μ_B. Parameters corresponding to Mn^{2+} were used for calculating the magnetic form-factor. An overall scale factor and the level of a constant background were refined. A separate scale factor for the magnetic contribution to the model scattering was varied in order to account for

deviations from the nominal effective moment. The impurity phases (see Phase analysis section) were accounted for by generating total scattering “experimental” data using the RMCPOW program, with configurations based on the corresponding structural parameters from the Rietveld refinements. These data sets were used as additional “backgrounds” with refinable scale factors. At convergence, 20 statistically independent configurations were collected for each temperature, with on average two moves per spin between each saved configuration. All results below are based on mean observations from these configurations.

In analogy to atomic diffuse scattering, magnetic SRO can be characterized by a spin-spin pair correlation function, m(r), which measures average spin correlations at various interatomic distances r. Here m(r) is defined as the sum of dot products of the spin unit vectors divided by the number of pairs at distance r, so that $-1 \leq m(r) \leq 1$. Thus, for $m(r) = -1$ all pairs of spins with distance r have complete anti-parallel alignments.

Electron diffraction

Samples for the electron diffraction studies were ground under butanol and a drop of the resulting suspensions were placed onto a holey carbon film supported by a copper grid. The electron diffraction patterns were obtained with a Philips 430 transmission electron microscope operating at 300 kV equipped with a LINK AN10000 analysis system.

Magnetization measurements

A Quantum Design MPMSXL5 super conducting quantum interference device (SQUID) magnetometer was used to measure the magnetic response as a function of temperature and applied magnetic field. Magnetization vs. field was measured in the range -10 kOe to 10 kOe at temperatures 10 K, 60 K and 300 K. The temperature dependence of the magnetization was

measured using zero field cooled (ZFC) and field cooled (FC) protocols, in the temperature range 10–400 K in applied fields of 10 and 1500 Oe.

Results and discussion

Phase analysis

The majority of the lines in x-ray powder diffraction films can be indexed by a face centered cubic unit cell, with the lattice parameter a = 12.0141(2) Å, suggesting that the compound can be classified as a G-phase [28,29]. The remaining lines are explained by Pd_2Si and Mn_5Si_3, estimated to about 2 % and 1 %, respectively, in mass of the sample in quantitative phase analysis of neutron powder diffraction data. The unit cell volume of the main phase (G-phase) varies less than 0.1 % between samples of different compositions and small amounts of Pd_2Si and/or Mn_5Si_3 are always present, which indicates a limited range of homogeneity. However, the metallic radii of Mn and Pd are very similar (1.37 Å and 1.38 Å, respectively), and the possibility of a certain range of solid solubility can not be excluded, despite the very small unit cell volume variation.

Crystal structure

The crystal structure can be described in space group $Fm\bar{3}m$, with 120 atoms distributed over six non-equivalent crystallographic sites. The solution that best fits the observed intensities of all data sets is to have mixed occupancies of manganese and palladium in three metal sites (*32f*, *32f*, *4a*), whereas the fourth metal site (*24e*) is fully occupied by manganese. Full occupancy of silicon was found for the *24d* and *4b* sites. The obtained occupancies approximately correspond to the composition $Mn_8Pd_{15}Si_7$. The crystal structure parameters, obtained in the last cycles of refinements on neutron powder diffraction intensities, are listed

in Table 1, and the neutron powder diffraction profile is shown in Fig. 2. Table 2 shows interatomic distances shorter than 3.7 Å.

The atom positions of $Mn_8Pd_{15}Si_7$ correspond to those of the binary $Sc_{11}Ir_4$ type structure [30] and of the ternary compound $Zr_6Zn_{23}Si$ [31]. These are derived from the Th_6Mn_{23} [32] and $Mg_6Cu_{16}Si_7$ type structures [9,10], by filling the octahedral void in the *4a* site[†]. The individual coordination polyhedra of $Mn_8Pd_{15}Si_7$ are illustrated in Fig. 3. The M1, M2 and M4 atoms have irregular coordination polyhedra of 12, 13, and 9 atoms, respectively. Both Si1 and Si2 are coordinated by cubes of M1 and M2 atoms, distorted in the case of Si1, and a perfect cube for Si2. Finally octahedra of Mn atoms (M4 site) surround the M3 position. The complete crystal structure can be built from three of these polyhedra: Mn_6-octahedra, placed at the corners and face centers of the unit cell, surrounded by octahedron shaped shells of edge sharing cubes of Si1 and Si2 coordination polyhedra, as shown in Fig. 4. For more in-depth descriptions of filled Th_6Mn_{23} related structures, see e.g. Refs. [30] and [33].

To illustrate where magnetic interactions between neighboring manganese atoms can take place, links between the metal sites have been introduced in Fig. 5 (for clarity showing only one eighth of the unit cell content). The shortest Mn–Mn distance (2.57 Å) is found between the Mn atoms on the corners of the octahedra (M4; 100 % Mn) and Mn atoms in the center of the octahedra (M3; 16 % Mn). M1 atoms (6 % Mn) cap the octahedron faces, forming M1–M4 links (2.78 Å), whereas one M2 atom (21 % Mn) links to three M4 atoms (2.83 Å) on different octahedra. The distance between fully Mn occupied sites (M4–M4; on the edges of the octahedra) is considerably longer (3.64 Å).

[†] Our assignment of the *4a* site corresponds to that originally cited for Th_6Mn_{23} by Florio *et al.* [32] and also used in Refs. [9,30,31]. In contrast, in Refs. [33-36] this is assigned as the *4b* site, with an associated translation of the origin by (½, ½, ½) affecting the coordinates of the other sites.

There are several examples in the literature where mixed occupancy is observed in filled Th_6Mn_{23} type structures. Grytsiv *et al.* [34,35] reported mixed occupancy of several metal sites for G-phases of the approximate formula $TiMAl_{\sim 2}$ (M = group 8-10 transition metal). Ding *et al.* [36] reported the τ_2-$(Ti,Al)_6(Ti,Pd/Pt,Al)_{23+1}$ phase, for which the composition of the limited solid solubility range does not agree with the stoichiometry of the adopted structure type, and the crystal structure displays mixed metal site occupancy. Numerous examples of so called G-phases, classified by the dimension and fcc symmetry of the unit cell, are provided in the literature for ternary intermetallic silicides and germanides of the general formula $T_6T_{16}(Si/Ge)_7$ [28,37] as well as for aluminides, zincides and beryllides of the general formula $T_6T_7Al_{16}$, T being transition metals [29,38]. However, the exact composition and atom positions are often not given, and could correspond to either the $Mg_6Cu_{16}Si_7$ type or the filled Th_6Mn_{23} type structure, possibly with mixed site occupancies.

Electron Diffraction

If a crystal structure refinement results in an average structure with mixed atomic sites, then an electron microscopy study often reveals additional ordering evidenced by electron scattering additional to the Bragg reflections of the average cell (or lower than expected local symmetry). However in this case, neither satellite reflections (indicating long range ordering of the atoms on these sites), nor clearly localized diffuse electron scattering (indicating short range ordering) could be observed.

No deviations from the $Fm\bar{3}m$ symmetry could be detected. Instead a *subcell* with $\mathbf{a}_s = ½\ \mathbf{a}$ could sometimes be found, seemingly also with the $Fm\bar{3}m$ symmetry. This phase is coherently interwoven with the main phase and could only be found very scarcely. The phase

was observed by using a small aperture or a converged beam and by carefully studying the intensities of the reflections from this sublattice and comparing them to the intensities of the superstructure reflections (i.e. reflections from only the main phase) while moving the crystallite in the beam. Sometimes the electron beam could be focused on only this minor phase and then the superstructure reflections (i.e. reflections from only the main phase) were absent, thus proving that there is indeed a separate phase distributed as small domains with a diameter of maximum 1000 Å. The powder X-ray and neutron diffraction patterns show no evidence of this phase and we assume at this stage that the amount of this phase is too small to give any quantifiable contribution to the powder diffraction patterns.

A certain range of solid solubility is suggested by the preliminary electron microscopy study, as contrast variations and variations in composition from EDX analyses were observed although not quantified.

Magnetic susceptibility

In Fig. 6 magnetic susceptibility curves M(T)/H at two different applied magnetic fields (10 and 1500 Oe) are shown. The magnetization has been measured by both zero field cooled (ZFC) and field cooled (FC) protocols. There is quite a lot of structure in these magnetization curves, and also a significant non-linearity with field. Fig. 7 shows magnetization vs. field curves at three different temperatures. The curves at 10 K and 60 K show a weak ferromagnetic response with a saturation moment of about 2 emu/g superposed on a 'paramagnetic' background signal. The magnetization curve at 300 K is still non-linear but has a much lower slope ('susceptibility').

Looking back to Fig. 6, and considering first the low field results, one can assign the anomaly at about 40 K (giving rise to an increased irreversibility between the low field ZFC and FC curves) to a spin glass like ordering of the main phase. The onset of irreversibility in the 10 Oe curves occurring at about 100 K may be due to the impurity phase Mn_5Si_3, which orders in an antiferromagnetic (AF) structure at 99 K. The reason for the irreversibility is then that an excess magnetization appears at the AF transition due to uncompensated spins at the surface (and at domain walls) of the inclusions of Mn_5Si_3. At higher temperatures the behavior is quite anomalous: A broad maximum is followed by two broad knees around 150 K and 250 K and finally at high temperatures the magnetization seems to decay quite regularly. Corresponding, but less pronounced features are observed in the high field (1500 Oe) curve.

In Fig. 8 the inverse of M/H is plotted vs. T at higher temperatures. For the 1500 Oe curve, a Curie-Weiss behavior may be distinguished in the temperature range 320–400 K, yielding $\theta \approx 260$ K and a p_{eff} of 3.5 μ_B/Mn. The positive value of θ indicates ferromagnetic interaction and this is also corroborated by the non-linear M vs. H curves. It is, on the other hand, a conclusion that contrasts with the dominating antiferromagnetic character of the spin structure that the low temperature neutron diffraction data suggest. The spin glass like transition that occurs at about 40 K supports, however, that competition between antiferro and ferromagnetic interaction does occur in the system.

Magnetic short-range order

In the neutron diffraction data, in addition to the nuclear Bragg peaks and (mainly thermal) diffuse scattering, there is a broad bump at $2\theta \approx 20°$ and also an upturn at low angles in the diffuse scattering, see Fig. 2. These features sharpen at low T and are thus most probably of

magnetic origin. However, since no new Bragg peaks appear, the ordering only takes place on a local scale. RMCPOW simulations were performed to model this SRO. The low-angle part, up to $2\theta = 80^{o}$, was used in the modeling. At higher angles the magnetic scattering contribution is insignificant due to the fast decrease of the magnetic form-factor. The only allowed type of move was spin rotation. Results of one converged model fitted to NPD data are shown in Fig. 9. Comparable values for the magnetic scale factor were found at all temperatures, showing that the effective moments and degree of localization of the spins do not change. The resulting scale factor indicated an effective moment of about 4 μ_B, i.e. close to the value found by the susceptibility measurements. The scale factors for the contribution from the impurity phases were also found to change little with temperature. With contributions of about 2% (Pd_2Si) and 1% (Mn_5Si_3) with respect to the total experimental cross-section we can safely ignore any influence on the main phase SRO. These aspects, in particular the general shape and magnitude of magnetic diffuse scattering, were well confirmed by the SLAD data.

From the fitted configurations the Mn–Mn partial spin-spin pair correlation functions, m(r), were calculated, and are shown in Figs. 10 and 11. The relative numbers of Mn at different sites indicate that only pairs involving M4 atoms make a significant contribution to the model scattering cross-section. For illustration of the different pairs, see Fig. 5. From the m(r) graphs it can be seen that for the M1/M2/M3–M4 1st nearest neighbors (NN) (< 3 Å), and at low temperature the M4–M4 1st NN pairs at 3.64 Å, the main features are antiferromagnetic (AFM) alignments, presumably because of dominant AFM interactions. The relatively smaller average alignment of M4–M4 1st NN pairs compared to M1/M2/M3–M4 pairs can be explained by the fact that AFM interactions on an octahedron are geometrically frustrated. Even in ordered systems the frustration leads to spin arrangements where m(r) does not

amount to -1 (corresponding to perfect AFM alignment). For example, in $Mn_6Ni_{16}Si_7$ [8], with unequal numbers of spins in the up and down direction, m(r) = -⅓; in Mn_3Pt [7], with non-collinear spins (Fig. 1b), m(r) = -½. The M4–M4 1st NN AFM correlation appears to vanish at 295 K, which indicates a weaker AFM magnetic interaction than for the Mn–Mn interactions at shorter distances.

At interatomic manganese distances of ~5 Å, mostly FM alignments are observed. Regarding the M4–M4 3rd NN pairs at 5.15 Å, *within* an octahedron, this could be explained by the intervening M3–M4 1st NN, apparently AFM, correlation, and/or also by the indirect ordering due to AFM M4–M4 1st NN correlations. The relatively stronger FM coupling of M4–M4 2nd NN pairs at 4.95 Å (between Mn on *different* octahedra) on the other hand is probably a result of the intervening AFM interaction of M2–M4 1st NN pairs. Beyond the second neighbor shell (distances > 5.5 Å) spin correlations in general become negligible.

RMC simulations generally tend to produce the most disordered configurations compatible with the data fitted. Additional simulations were therefore performed in order to check if there was some hidden order in the partial contributions to the model scattering cross-sections. A combination of the RMC fit to the diffraction data and standard Monte Carlo minimization of Heisenberg interactions was used and various attempts were made in which specific types of Mn pairs were forced to have FM or AFM interactions. The simulations with forced AFM 1st NN interactions showed a qualitative agreement with the un-constrained results presented above. This was expected since the un-constrained configurations already show AFM 1st NN alignment. The agreement with the data was almost as good and the overall tendencies of the spin-pair correlations (for significant pair types and distances) were the same.

Simultaneous FM average correlations of two or more of the significant pair types imposed long-range FM order and thus agreement with the diffraction data was very poor. In contrast, models with only one type of forced FM pair could be fitted reasonably well to the experimental data set. For models with forced FM M1–M4 interactions the imposed FM alignment was compensated by stronger AFM correlations of the M2–M4 correlations or vice versa. Other m(r) features were however again in qualitative agreement with the un-constrained model. Similar effects were observed for models with forced M3–M4 FM interactions. On the other hand, forced M4–M4 1st NN FM interactions resulted in a model, where the M4 spins could align to a high degree, and most M2–M4 1st NN pairs show strong AFM correlations. These two correlations produce strong alignment of spins on neighboring octahedra, so that ferrimagnetic clusters with M2 and M4 spins in opposite directions are obtained, with a correlation length of ~10 Å.

The lack of long-range magnetic order in $Mn_8Pd_{15}Si_7$ can be compared to the anti-ferromagnetically ordered $Mn_6Ni_{16}Si_7$ [8]. The inter- and intra-octahedron distances are not very different in the two crystal structures and it may be argued that the octahedra would tend to similar magnetic order. One important difference between the two structures is the random distribution of Mn atoms on the M1, M2 and M3 sites for $Mn_8Pd_{15}Si_7$. These manganese atoms cause magnetic frustration, which probably inhibits long-range magnetic ordering. With a strong AFM M3–M4 1st NN interaction, the role of M3 would presumably be to polarize the surrounding M4 atoms into a FM-like arrangement. The Mn atoms at the M1 and M2 sites interact antiferromagnetically with neighboring M4 atoms, which causes effective FM links from one octahedron to another (M2) or within an octahedron (M1). In $Mn_6Ni_{16}Si_7$ [8], where there are no magnetic atoms in-between the octahedra, the inter-octahedron coupling is clearly dominated by AFM interactions, as judged from the overall AFM

arrangement. It is reasonable to assume that in $Mn_8Pd_{15}Si_7$ the interaction between M4 atoms on neighboring octahedra is of an AFM character when there are no intermediate Mn atoms at the M2 site (21 % Mn / 79 % Pd). Since we by this argument would have both FM and AFM interactions between the Mn_6-octahedra (with and without Mn in the M2 site, respectively), the system is frustrated and magnetic long-range order is not achieved.

Finally, an attempt was also made to investigate possible atomic short-range order. In these simulations the positions of Mn and Pd atoms in randomly selected pairs (at M1, M2 or M3 sites) could be swapped, in addition to the spin rotation moves. The most apparent change that emerged from these simulations was an almost complete exclusion of Mn 1st NN on M1 and M2 sites, which corresponds to fluctuations in the nuclear diffuse scattering extending over the whole experimental range. Similar improvement was observed also with the SLAD data. However, as the largest amplitude of these oscillations is obtained at almost the same position as the main magnetic diffuse peak, the change in the model nuclear scattering almost completely cancels the corresponding change in the magnetic contribution. The observed minor improvement in the fit, compared to the random Mn/Pd distribution, could possibly be verified by polarized neutron studies. The absence of such SRO in the electron scattering data may be explained by the relatively smaller contrast of the Mn and Pd electron form-factors; both tend to about 7.5 Å for $Q = 4\pi \sin\theta / \lambda = 0$ and even at $Q = 10$ Å^{-1} the Pd/Mn form-factor ratio is ~1.5:1.0. Interestingly, the presence or not of atomic SRO does not seem to affect the qualitative interpretation of the spin structure as discussed above, e.g. M2–M4 correlations remain predominantly AFM. No atomic SRO was observed for M3 atoms.

Conclusions

A new G-phase, of the approximate formula $Mn_8Pd_{15}Si_7$, has been identified and found to crystallize in the $Sc_{11}Ir_4$ type structure, a filled version of the Th_6Mn_{23} and $Mg_6Cu_{16}Si_7$ type structures. Octahedra of manganese atoms, filled with a mixed Pd/Mn site, are found at the corners and face centers of the unit cell, with further mixed Pd/Mn sites capping and linking the octahedra and providing a random distribution of additional short Mn–Mn distances. No evidence of short-range or long-range order in the Pd/Mn distribution over the mixed metal sites was seen in electron diffraction.

Magnetic short-range order was modeled by Reverse Monte Carlo simulations. Within 3 Å separation, pairs of manganese atoms show dominating antiferromagnetic correlations. Weaker tendencies for antiferromagnetic interactions were found between Mn atoms on the octahedron edges. An alternative model, with small local ferrimagnetic clusters (a couple of Mn octahedra) fits the model reasonably well and would to some extent explain the small net magnetic moment of 2 emu/g found in magnetization measurements.

Since the Mn atoms form octahedra, the triangular geometry of the octahedron faces gives rise to geometric frustration of antiferromagnetic interactions. We suggest that the geometric frustration and, more importantly, the random distribution of additional Mn–Mn magnetic interactions with partly Mn occupied sites (for example on links between the octahedra, 21 % occupied by Mn) are important factors behind the observed lack of long-range magnetic order.

Acknowledgements

Håkan Rundlöf is acknowledged for skilful assistance in neutron powder diffraction data collection. Financial support from the Swedish Research Council (VR) and the Swedish Foundation for Strategic Research (SSF) is acknowledged.

References

[1] T. Eriksson, R. Lizárraga, S. Felton, L. Bergqvist, Y. Andersson, P. Nordblad and O. Eriksson, Phys. Rev. B 69 (2004) 054422.

[2] T. Eriksson, L. Bergqvist, P. Nordblad, O. Eriksson and Y. Andersson, J. Solid State Chem. 177 (2004) 4058-4066.

[3] J. S. Kouvel, J. S. Kasper, Proceedings of the International Conference on Magnetism, Nottingham 1964, Institute of Physics & Physical Society, London, 1965, pp 169.

[4] E. Kren, G. Kádár, L. Pál, J. Sólyom and P. Szabó, Phys. Lett. 20 (1966) 331-332.

[5] E. Krén, G. Kádár, L. Pál, J. Sólyom, P. Szabó and T. Tarnóczi, Phys. Rev. 171 (1968) 574-585.

[6] I. Tomeno, H. N. Fuke, H. Iwasaki, M. Sahashi and Y. Tsunoda, J. Appl. Phys. 86 (1999) 3853-3856.

[7] T. Ikeda and Y. Tsunoda, J. Phys. Soc. Jpn. 72 (2003) 2614-2621.

[8] M. Kolenda, A. Szytuła, J. Leciejewicz and C. Maletka, J. Magn. Magn. Mater. 96 (1991) 121-124.

[9] G. Bergman and J. L. T. Waugh, Acta Crystallogr. 9 (1956) 214-217.

[10] G. Nagorsen and H. Witte, Z. Anorg. Allg. Chem. 271 (1953) 144.

[11] R. L. McGreevy, J. Phys.: Condens. Matter 13 (2001) R877-R913.

[12] A. Mellergård and R. L. McGreevy, Acta Crystallogr. A 55 (1999) 783-789.

[13] A. Mellergård and R. L. McGreevy, Mat. Sci. Forum 71 (2001) 378-381.

[14] A. Mellergård and R. L. McGreevy, J. Phys.: Condens. Matter 10 (1998) 9401-9412.

[15] A. Mellergård, C. Mondelli, H. Mutka, R. L. McGreevy and C. Payen, Appl. Phys. A 74 (2002) S883-S885.

[16] A. Mellergård, R. L. McGreevy and S.-G. Eriksson, J. Phys.: Condens. Matter 12 (2000) 4975.

[17] D. Sanchez, J. A. Alonso, M. Garcia-Hernandez, M. J. Martinez-Lope, J. L. Martinez and A. Mellergård, Phys. Rev. B 65 (2002) 104426.

[18] A. K. Azad, A. Mellergård, S.-G. Eriksson, S. A. Ivanov, J. Eriksen and H. Rundlöf, Appl. Phys. A 74 (2002) S763-S765.

[19] J. R. Stewart and R. Cywinski, J. Magn. Magn. Mater. 272-276 (2004) 676-678.

[20] S. Rundqvist, Chem. Scr. 28 (1988) 15-20.

[21] SHELX-97, Bruker AXS, Madison, Wisconsin, USA (2004).

[22] J.-O. Lundgren, Crystallographic computing programs. Report UUIC-B14-405, Institute of Chemistry, Uppsala University, Sweden, 1983.

[23] P. S. Salmon, J. Phys. F: Met. Phys. 18 (1988) 2345-2352.

[24] M. A. Howe, CORRECT computer program. Program and manual can be downloaded from ftp://ftp.studsvik.uu.se.

[25] J. Rodríguez-Carvajal, FULLPROF computer program, version 2.80, LLB, Saclay (2004).

[26] A. Nylund, Acta Chem. Scand. 20 (1966) 2381-2386.

[27] B. Aronsson, Acta Chem. Scand. 14 (1960) 1414-1418.

[28] F. X. Spiegel, D. Bardos and P. A. Beck, Trans. Met. Soc. AIME 227 (1963) 575-579.

[29] E. Ganglberger, H. Nowotny and F. Benesovsky, Monatsh. Chem. 97 (1966) 219-220.

[30] B. Chabot, K. Cenzual and E. Parthé, Acta Crystallogr. B 36 (1980) 7-11.

[31] X. Chen, W. Jeitschko and M. H. Gerdes, J. Alloys Compd. 234 (1996) 12-18.

[32] J. V. Florio, R. E. Rundle and A. I. Snow, Acta Crystallogr. 5 (1952) 449-457.

[33] H. G. von Schnering, R. H. Cardoso Gil, W. Hönle, N. Caroca-Canales and K. Peters, Z. Anorg. Allg. Chem. 622 (1996) 112-122.

[34] A. Grytsiv, J. J. Ding, P. Rogl, F. Weill, B. Chevalier, J. Etourneau, G. André, F. Bourée, H. Noël, P. Hundegger and G. Wiesinger, Intermetallics 11 (2003) 351-359.

[35] A. Grytsiv, P. Rogl, H. Schmidt, G. Giester, P. Hundegger, G. Wiesinger and V. Pomjakushin, Intermetallics 12 (2004) 563-577.

[36] J. J. Ding, P. Rogl, B. Chevalier and J. Etourneau, Intermetallics 8 (2000) 1377-1384.

[37] E. I. Gladyshevskii, P. I. Kripyakevich, Y. B. Kuz'ma and M. Y. Teslyuk, Sov. Phys. Crystallogr. 6 (1961) 615-620 (translated from: Kristallografiya, 6 (1961) 769).

[38] E. Ganglberger, H. Nowotny and F. Benesovsky, Monatsh. Chem. 97 (1966) 829-832.

Table 1. Final structural parameters at 295 K. Estimated standard deviations in parentheses.

Space group: $Fm\bar{3}m$, unit cell parameter: a = 12.0141(2) Å.

Atom	*Wyckoff site*	*x*	*y*	*z*	*occupancy*
M1	*32f*	0.15859(9)	0.15859(9)	0.15859(9)	94 % Pd 6 % Mn
M2	*32f*	0.3842(1)	0.3842(1)	0.3842(1)	79 % Pd 21 % Mn
M3	*4a*	0	0	0	84 % Pd 16 % Mn
M4	*24e*	0.2145(2)	0	0	100 % Mn
Si1	*24d*	0	¼	¼	100 % Si
Si2	*4b*	½	½	½	100 % Si
$B_{overall}$ (Å^2)	0.72(1)				
R_p = 3.44 %; R_{wp} = 4.44 %; R_{exp} = 3.13 %; χ^2 = 2.01; R_{Bragg} = 5.21 %					

Table 2. Interatomic distances < 3.7 Å. Estimated standard deviations in parentheses.

Atom	*Atom*	*Distance (Å)*	*Atom*	*Atom*	*Distance (Å)*
M1	3 Si1	2.457(1)	M4	M3	2.57(3)
	3 M4	2.78(1)		4 M1	2.78(1)
	3 M2	2.81(2)		4 M2	2.83(2)
	3 M1	3.10(2)		4 Si1	3.033(4)
	M3	3.30(2)		Si2	3.43(3)
M2	Si2	2.41(3)		4 M4	3.64(4)
	3 Si1	2.67(1)	Si1	4 M1	2.457(1)
	3 M2	2.78(2)		4 M2	2.67(1)
	3 M1	2.81(2)		4 M4	3.033(4)
	3 M4	2.83(2)	Si2	8 M2	2.41(3)
M3	6 M4	2.57(3)		6 M4	3.43(3)
	8 M1	3.30(2)			

Figure captions

Fig. 1 (a) Geometric frustration of antiferromagnetic interactions on an octahedron. (b) The magnetic structure (120° spin arrangement) of Mn_3Rh, Mn_3Ir and Mn_3Pt (D-phase).

Fig. 2. Observed (points), calculated (solid line), and difference (observed-calculated; bottom solid line) neutron powder diffraction profiles at 295 K. Tick marks show the positions of Bragg reflections for $Mn_8Pd_{15}Si_7$ (upper set), Pd_2Si (middle set), and Mn_5Si_3 (lower set). Inset shows the increased background curvature at low temperature: a magnified section of the low angle data at 10 K (upper profile, with intensity scale offset) and at 295 K (lower profile).

Fig. 3. Coordination polyhedra around (a) M1 atoms, (b) M2 atoms, (c) M3 atoms, (d) M4 atoms, (e) Si1 atoms, (f) Si2 atoms.

Fig. 4. The crystal structure of $Mn_8Pd_{15}Si_7$, emphasizing the Mn (M4) octahedra around the M3 atoms, and the octahedron shaped shell of edge sharing Si1 (lighter) and Si2 (darker) coordination cubes. Numbers 1–4 are assigned to atom positions M1–M4.

Fig. 5. One eighth of the unit cell, Si atoms not shown. Inserted links illustrate possible magnetic exchange interactions between manganese atoms.

Fig. 6. Susceptibility (χ = M/H) vs. temperature, measured in the applied fields H = 10 Oe and H = 1500 Oe, respectively.

Fig. 7. Magnetization vs. field curves measured at temperatures 10 K, 60 K, and 300 K, respectively.

Fig. 8. Inverse susceptibility vs. temperature plot. Line shows the fit to Curie-Weiss type behavior of data measured in the applied field H = 1500 Oe.

Fig. 9. RMCPOW fit to the 10 K data. (o) Experimental data; (solid line) total RMC model scattering; (thick solid line) model magnetic scattering; (dashed line) nuclear diffuse scattering. The data to model difference is also shown (bottom solid line).

Fig. 10. Selected Mn–Mn partial spin-pair correlation functions at 10 K.

Fig. 11. Temperature dependence of the spin-pair correlation for some of the first and second Mn–Mn neighbor pairs.

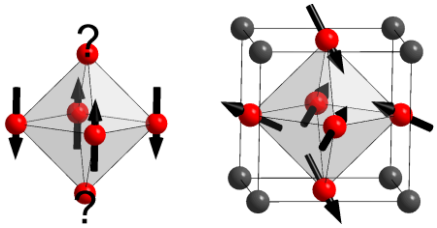

(a) (b)

Fig. 1 (a) Geometric frustration of antiferromagnetic interactions on an octahedron. (b) The magnetic structure (120° spin arrangement) of Mn_3Rh, Mn_3Ir and Mn_3Pt (D-phase).

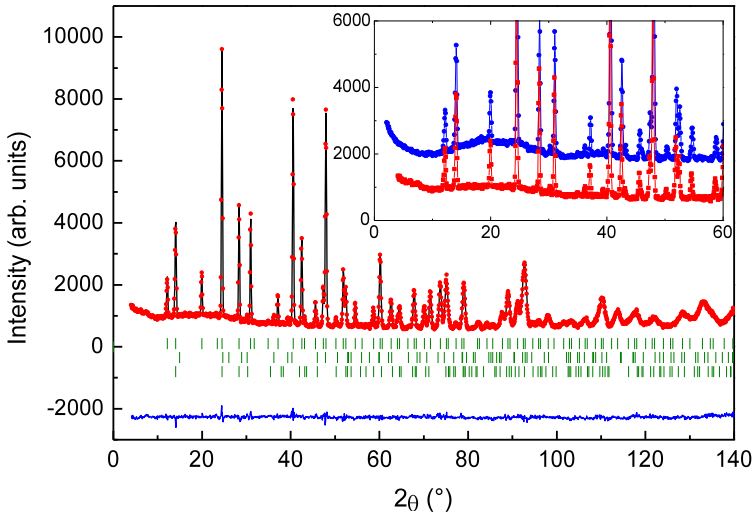

Fig. 2. Observed (points), calculated (solid line), and difference (observed-calculated; bottom solid line) neutron powder diffraction profiles at 295 K. Tick marks show the positions of Bragg reflections for $Mn_8Pd_{15}Si_7$ (upper set), Pd_2Si (middle set), and Mn_5Si_3 (lower set). Inset shows the increased background curvature at low temperature: a magnified section of the low angle data at 10 K (upper profile, with intensity scale offset) and at 295 K (lower profile).

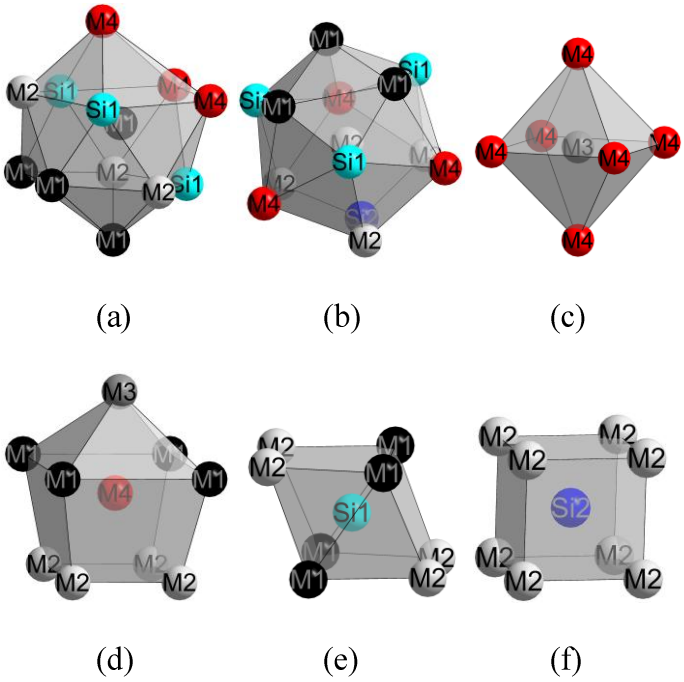

Fig. 3. Coordination polyhedra around (a) M1 atoms, (b) M2 atoms, (c) M3 atoms, (d) M4 atoms, (e) Si1 atoms, (f) Si2 atoms.

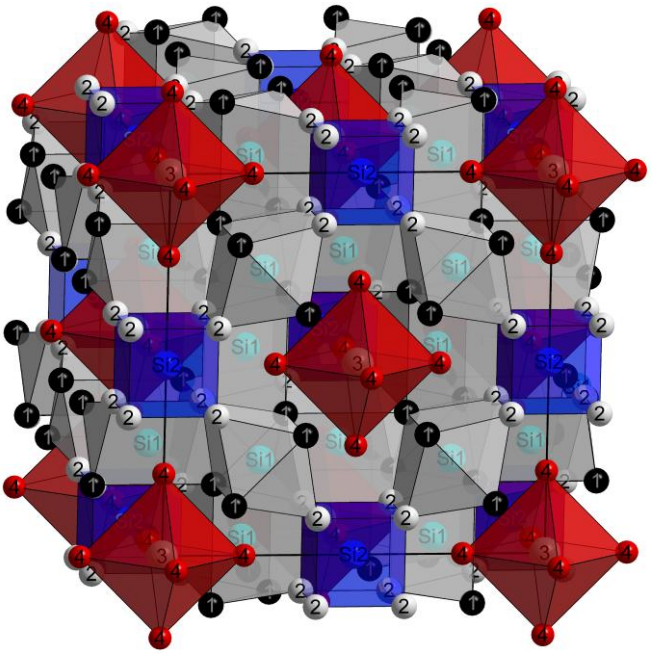

Fig. 4. The crystal structure of $Mn_8Pd_{15}Si_7$, emphasizing the Mn (M4) octahedra around the M3 atoms, and the octahedron shaped shell of edge sharing Si1 (lighter) and Si2 (darker) coordination cubes. Numbers 1–4 are assigned to atom positions M1–M4.

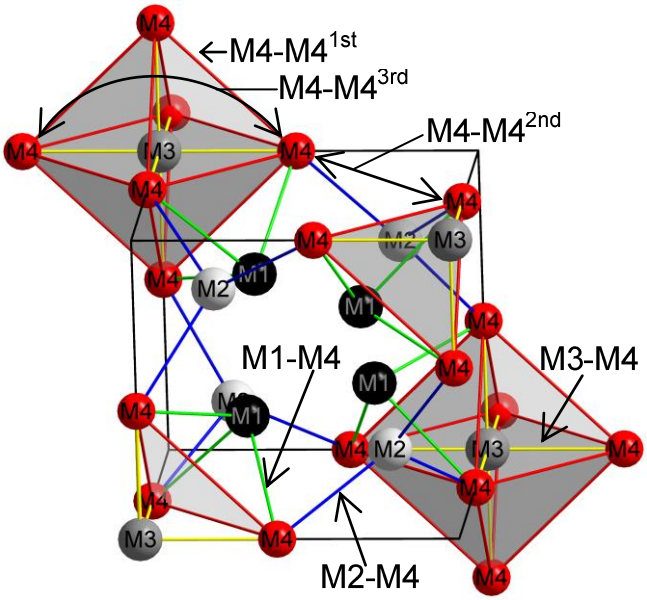

Fig. 5. One eighth of the unit cell, Si atoms not shown. Inserted links illustrate possible magnetic exchange interactions between manganese atoms.

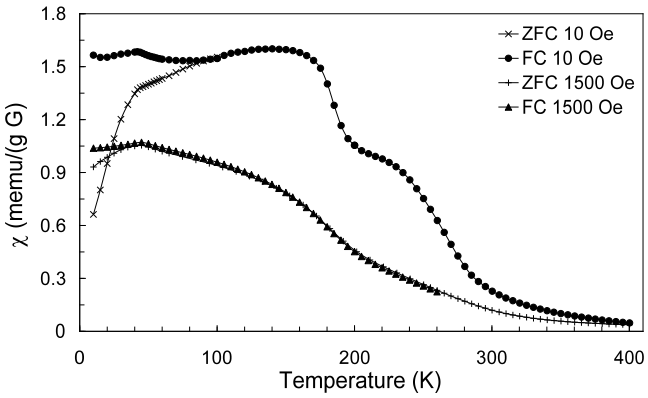

Fig. 6. Susceptibility (χ = M/H) vs. temperature, measured in the applied fields H = 10 Oe and H = 1500 Oe, respectively.

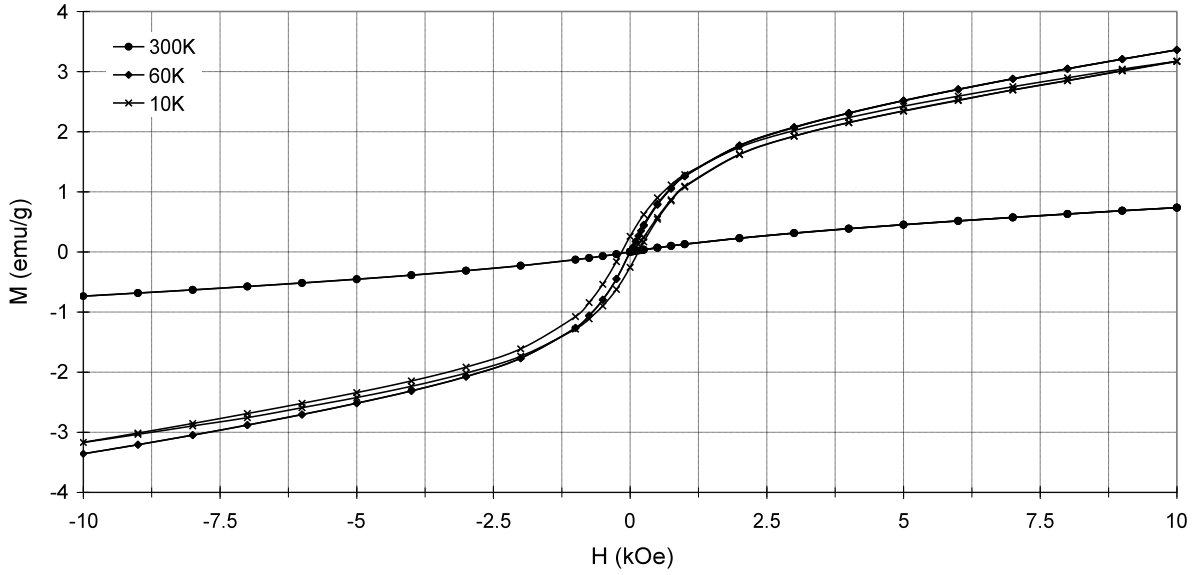

Fig. 7. Magnetization vs. field curves measured at temperatures 10 K, 60 K, and 300 K, respectively.

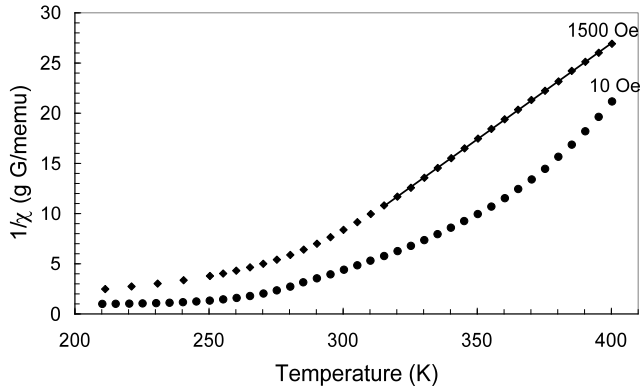

Fig. 8. Inverse susceptibility vs. temperature plot. Line shows the fit to Curie-Weiss type behavior of data measured in the applied field H = 1500 Oe.

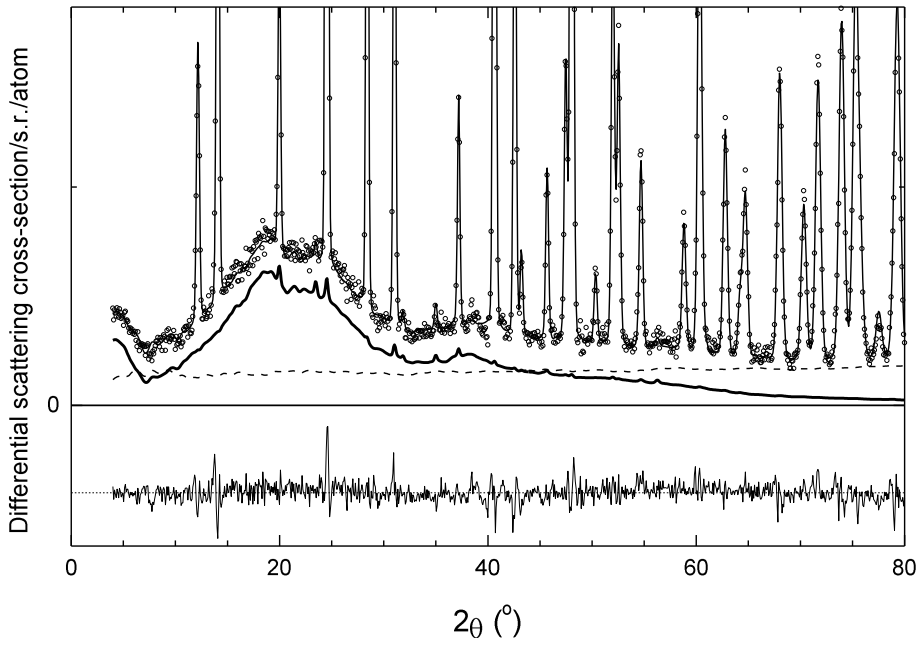

Fig. 9. RMCPOW fit to the 10 K data. (o) Experimental data; (solid line) total RMC model scattering; (thick solid line) model magnetic scattering; (dashed line) nuclear diffuse scattering. The data to model difference is also shown (bottom solid line).

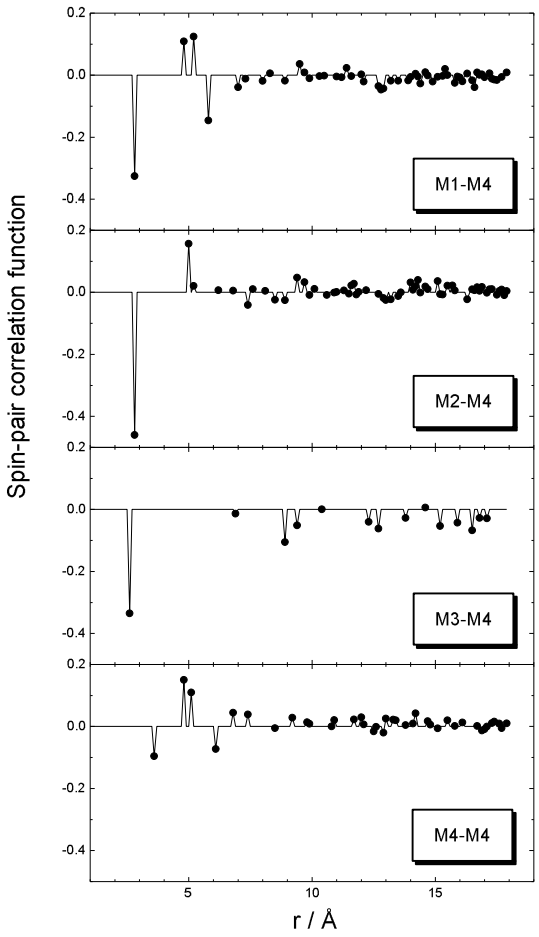

Fig. 10. Selected Mn–Mn partial spin-pair correlation functions at 10 K.

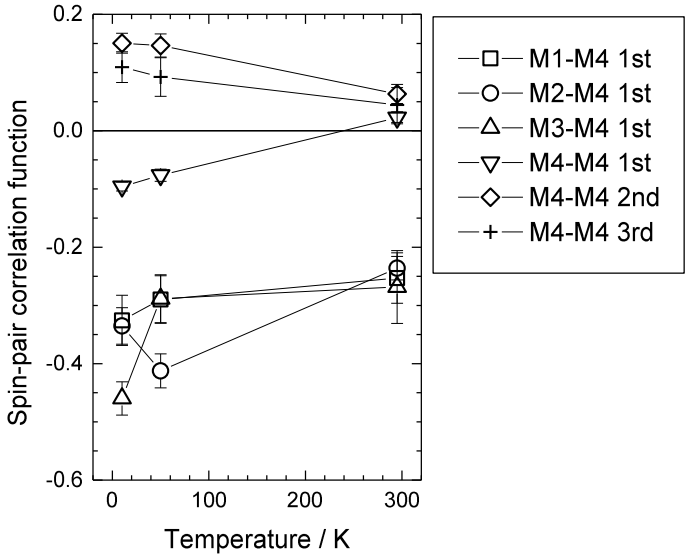

Fig. 11. Temperature dependence of the spin-pair correlation for some of the first and second Mn–Mn neighbor pairs.